ADVANCED MATERIALS
www.advmat.de

# Microstructured Polyelectrolyte Elastomer-Based Ionotronic Sensors with High Sensitivities and Excellent Stability for Artificial Skins

*Yi-ming Yuan, Binhong Liu, Mohammad Reza Adibeig, Qiqi Xue, Chu Qin, Qing-yin Sun, Ying Jin, Min Wang,* and Canhui Yang**

**High-performance flexible pressure sensors are highly demanded for artificial tactile sensing. Using ionic conductors as the dielectric layer has enabled ionotronic pressure sensors with high sensitivities owing to giant capacitance of the electric double layer (EDL) formed at the ionic conductor/electronic conductor interface. However, conventional ionotronic sensors suffer from leakage, which greatly hinders long-term stability and practical applications. Herein, a leakage-free polyelectrolyte elastomer as the dielectric layer for ionotronic sensors is synthesized. The mechanical and electrical properties of the polyelectrolyte elastomer are optimized, a micropyramid array is constructed, and it is used as the dielectric layer for an ionotronic pressure sensor with marked performances. The obtained sensor exhibits a sensitivity of 69.6 kPa$^{-1}$, a high upper detecting limit on the order of 1 MPa, a fast response/recovery speed of ≈6 ms, and excellent stability under both static and dynamic loads. Notably, the sensor retains a high sensitivity of 4.96 kPa$^{-1}$ at 500 kPa, and its broad sensing range within high-pressure realm enables a brand-new coding strategy. The applications of the sensor as a wearable keyboard and a quasicontinuous controller for a robotic arm are demonstrated. Durable and highly sensitive ionotronic sensors potentialize high-performance artificial skins for soft robots, human–machine interfaces, and beyond.**

## 1. Introduction

The mechanoreceptors in natural skins allow biological systems to feel and interact with the surroundings for environmental adaptation and survival. Artificial skins equipped with flexible pressure sensors emulate the functions of natural skins, enabling a wide range of applications as diverse as interactive robots,[1–4] prosthetics,[5–7] healthcare monitoring,[8–10] and virtual/augmented reality.[11] Among the many types of flexible pressure sensors, the capacitive sensor features a simple device structure, low energy consumption, fast response time, low detection limit, and excellent stability.[12] Conventional capacitive-type flexible pressure sensors suffer from low sensitivity and narrow pressure-response range.[13–15] Improvements have been made by using composite dielectric elastomer, e.g., doping carbon nanotubes into polydimethylsiloxane (PDMS) elastomer,[16,17] or architecting the interfacial structures of the dielectric elastomers.[16,18,19] Introducing microstructures to the dielectric elastomer enhances not only the sensitivity by increasing the compliance and the effective dielectric constant when subject to pressure but also the response speed by providing voids for elastic deformation.[18] However, due to the presence of the dielectric elastomer which is mostly incompressible and has a limited thickness on the order of 10 μm, the value of the capacitance is typically small (<100 pF),[15,20] limiting the sensitivity to the order of 1 kPa$^{-1}$.

The issues associated with the dielectric elastomer are readily resolved by using a layer of ionic conductors, which adopts mobile ions as the charge carriers. When an ionic conductor contacts an electronic conductor, ions and electrons (or holes) accumulate at the interface to form an electric double layer (EDL). The capacitance per unit area reaches ≈10$^{-2}$ F m$^{-2}$ since the EDL separates charges of opposite polarity at the nanometer scale.[21] During operation, the effective area of EDL increases in response to pressure, inducing an increment of the capacitance of the sensor. This new family of sensors is referred to as ionotronic (or iontronic) sensors because the sensing

Y.-ming Yuan, B. Liu, M. R. Adibeig, Q. Xue, C. Yang
Shenzhen Key Laboratory of Soft Mechanics & Smart Manufacturing
Department of Mechanics and Aerospace Engineering
Southern University of Science and Technology
Shenzhen 518055, P. R. China
E-mail: yangch@sustech.edu.cn

C. Qin, Q.-yin Sun, Y. Jin, M. Wang
School of Microelectronics
Southern University of Science and Technology
Shenzhen 518055, P. R. China
E-mail: wangm@sustech.edu.cn

M. Wang
Engineering Research Center of Integrated Circuits for Next-Generation Communications
Ministry of Education
Southern University of Science and Technology
Shenzhen 518055, P. R. China

The ORCID identification number(s) for the author(s) of this article can be found under https://doi.org/10.1002/adma.202310429

DOI: 10.1002/adma.202310429

 

mechanism relies on the synergy of ions and electrons.[22,23] Over the past decade, intensive efforts have been devoted to exploring ionotronic sensors with various ionic conductors, including ionic liquid droplets,[24] ionogels,[25,26] and ionic hydrogels.[27,28] Marvelous performances, such as extremely high sensitivities[29–30] and broad sensing ranges[28,31] have been achieved by constructing microstructures on the surface of the ionic conductors. However, liquid droplets[24] are prone to leakage and the reproducibility and reliability of the sensor are of concern; hydrogels are susceptible to the evaporation and leakage of water; and ionogels are vulnerable to the leakage of ionic liquid in addition to the controversial biocompatibility concern.[32,33] Therefore, fabricating ionotronic sensors with high sensitivities and excellent stability is crucial for the field but remains an unmet challenge.

Herein, using the photolithography technique and a solvent-free and leakage-free polyelectrolyte elastomer (PEE), we resolve the challenge by synthesizing a microstructured ionic conductor for highly sensitive and highly stable ionotronic sensors. We synthesize a polymerizable ionic monomer, copolymerize it with a neutral monomer, and tune the crosslink density to balance the mechanical and electrical properties of the PEE, which is mechanically stretchable, fatigue-resistant, ionically conductive, and ambiently stable. We construct micropyramids on one surface of the PEE by replicating the patterns of an etched silicon wafer and fabricate ionotronic sensors by sandwiching the microstructured PEE between two indium tin oxide (ITO) electrodes. The obtained ionotronic sensor achieves a high sensitivity of 69.6 $kPa^{-1}$, a high upper detecting limit on the order of 1 MPa, a fast response/recovery speed of ≈6 ms, and excellent stability under a static load of 100 kPa over 4000 s, a dynamic load of 300 kPa over 1000 cycles, and a dynamic load of 20% strain over 1000 cycles. Remarkably, the sensor retains a high sensitivity of 4.96 $kPa^{-1}$ at a high pressure of 500 kPa. Moreover, the ultrabroad sensing range enables a brand-new coding strategy in that the signal can be divided into multiple intervals, each corresponding to a command without signal interference. We demonstrate the applications of ionotronic sensors as a wearable keyboard and a wearable quasi-continuous controller for a robotic arm. Such high-performance ionotronic sensors have great potential in wearable electronics and systems.

## 2. Results and Discussion

The ionotronic sensor consists of a layer of microstructured PEE sandwiched by two electrodes with a spacer in between (**Figure 1a**). The top surface of PEE contains a micropyramid array and is separated from the top electrode by air at the undeformed state, while the bottom surface is in full contact with the bottom electrode, forming a constant EDL. Subject to a pressure, the top electrode is compressed to contact the tips of the micropyramid array, forming distributed EDLs. The effective capacitance of the distributed EDLs, $C_{EDL}$, is proportional to the contact area, which increases with pressure and plateaus when the micropyramids are flattened under a high pressure. The equivalent circuit of the sensor, when connected to a capacitance meter, contains two tunable capacitors due to the air $C_{air}$ and the distributed EDLs $C_{EDL}$ in parallel, which are in turn in series with a constant capacitor due to the bottom constant EDL, $C_{EDL0}$, and a resistor due to the bulk resistivity of PEE, $R_{PEE}$, (Figure 1b). At the undeformed state, the capacitance of the sensor is nearly the air capacitance because $C_{EDL0}$ is usually by orders of magnitudes larger than $C_{air}$. Under pressure, the capacitance of the sensor is dominated by the tunable capacitance $C_{EDL}$ when the pressure is low, $C_{air} << C_{EDL} << C_{EDL0}$, and approximates $(C_{EDL}{}^{-1} + C_{EDL0}{}^{-1})^{-1}$ when the pressure is high and the micropyramid arrays are mostly flattened.

To tackle the leakage issue, we design and synthesize a solvent-free PEE, i.e., poly (1-butyl-3-methylimidazolium 3-sulfopropyl methacrylate-*co*-methyl acrylate) (P([BMIM][SPA]-*co*-MA)), which contains anions fixed on the polymer network and mobile cations (Figure 1c). We first synthesize a polymerizable ionic monomer, [1-butyl-3-methylimidazolium] [3-sulfopropyl methacrylate] ([BMIM][SPA]), and then randomly copolymerize it with a neutral monomer, methyl acrylate (MA), using 1,6-hexanediol diacrylate (HDDA) as the covalent crosslinker. The chemical structures of P([BMIM][SPA]-*co*-MA) network are shown in Figure 1d. On one hand, the leakage of anions is inhibited by network elasticity; on the other hand, the leakage of cations is inhibited by electrostatic interactions.[34] The leakage issue can also be overcome by synthesizing PEEs with fixed cations and mobile anions[35,36] or zwitterionic monomers.[37,38] Because ionic moieties are generally hygroscopic, the introduction of hydrophobic MA helps mitigate the complications caused by the fluctuations in humidity. Furthermore, the short and nonpolar pendant groups of the MA segments, as well as the covalent crosslinks, are beneficial to the entropic elasticity of the polymer network, which is important to long-term stability.

To fabricate the ionotronic sensor, we cast the PEE precursor on a silicon substrate containing microsquare-pyramidal cavities, cure the precursor under UV illumination, peel the PEE off with complementary micropyramids, and sandwich the microstructured PEE by two ITO/PET electrodes with a ring-shaped PET as the spacer (Figure 1e). Figure 1f shows the array of the microsquare-pyramidal cavity on the silicon wafer. Figure 1g shows the array of micropyramids on the PEE. The sizes of the micropyramids are almost the same as those of the microsquare-pyramidal cavities, indicating high-fidelity of replicating. Figure 1h shows the appearance of an ionotronic sensor sealed by PET tapes.

The properties of PEEs underpin the performances of ionotronic sensors. In view that the mechanical properties of PEEs depend on the network structure and the electrical properties depend on the mobility of ions, we investigate the effects of crosslink density and the molar ratio between [BMIM][SPA] and MA on the mechanical and electrical properties of P([BMIM][SPA]-*co*-MA). The molar ratio of [BMIM][SPA] over MA of 1:3 balances the mechanical and electrical properties (Figure S1, Supporting Information) so that we fix this molar ratio and continue to tune the crosslink density. Crosslink density is defined as $n_{HDDA}/(n_{[BMIM][SPA]}+n_{MA})\times 100\%$, where $n$ represents the mole number and the subscript indicates the constituent. **Figure 2a** plots the uniaxial tensile stress–strain curves of different crosslink densities. The elastic modulus increases with the crosslink density, ranging from 301.6 to 675.5 kPa (Figure 2b). A lower elastic modulus gives a higher sensitivity for the ionotronic sensor,[15,29] and the moduli of all crosslink densities are much lower than the modulus of the commonly used PDMS elastomer, which is on the order of 1 MPa. The fracture strain decreases with

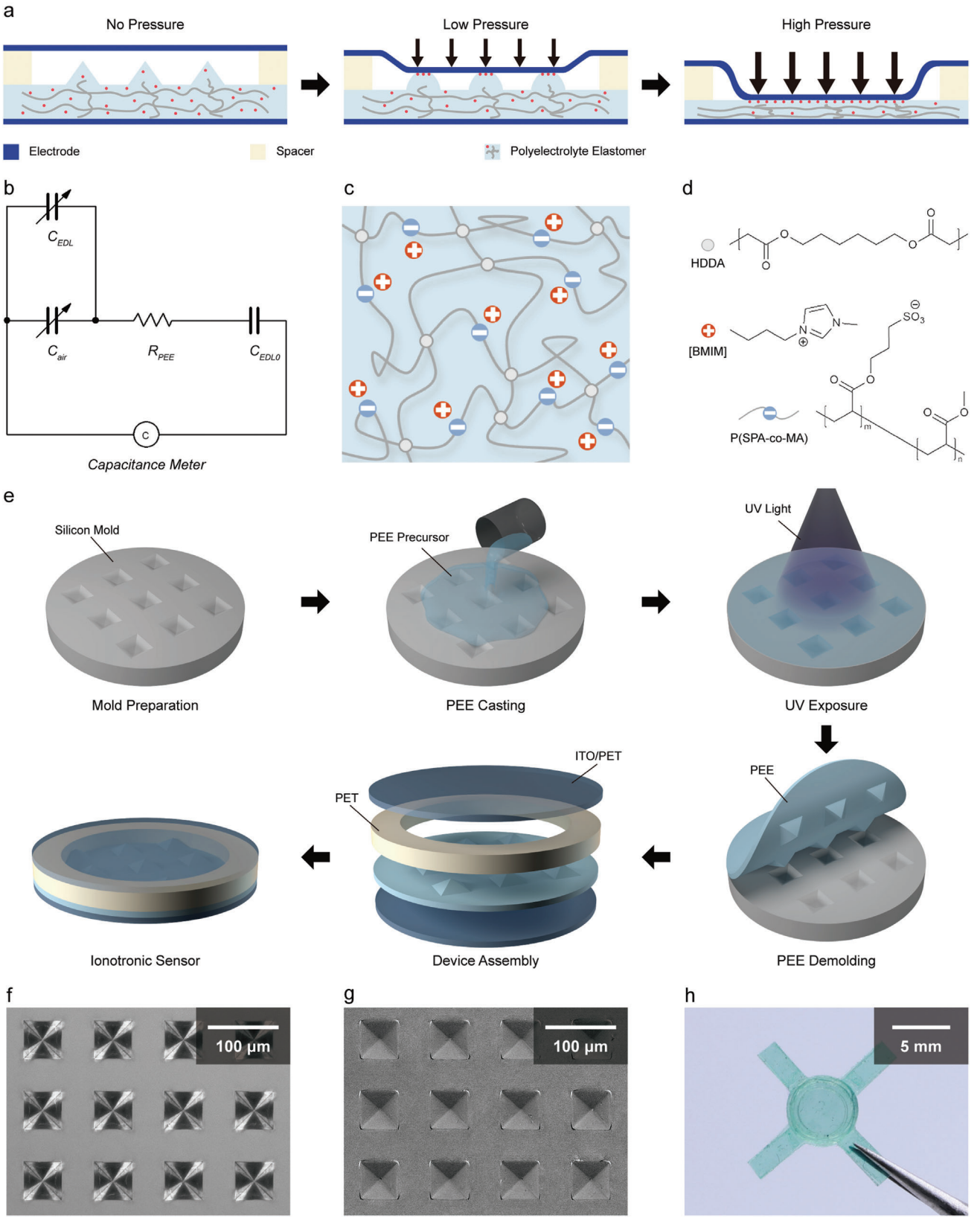


**Figure 1.** Principles, materials, and fabrication of the ionotronic sensor. a) Schematic of the working principle. b) Equivalent electric circuit. c) Schematic of the polymer network of the PEE. d) Chemical structures of the constituents. e) Schematic of the fabrication process. Top-view optical microscopic images of f) the microstructured silicon mold and g) the replicated microstructured PEE. h) Photograph of an ionotronic sensor.

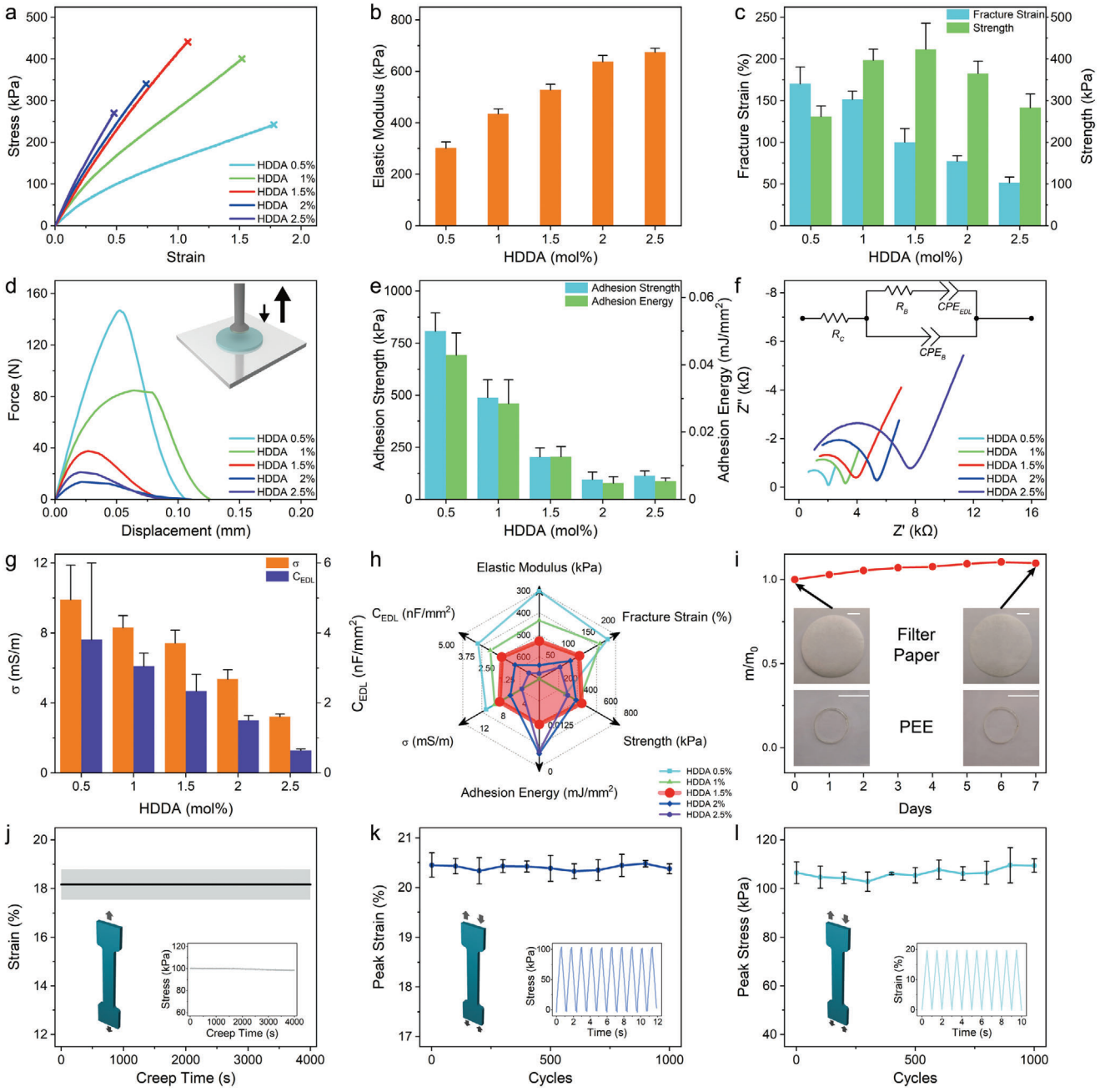


**Figure 2.** Mechanical and electrical properties of the PEE. a) Uniaxial tensile stress-strain curves. The variations of b) elastic modulus, c) fracture strain and strength with crosslink density. d) Force-displacement curves measured by the tack test as schematized in the inset. e) The variations of adhesion strength and adhesion energy with crosslink density. f) Nyquist plots of PEEs with different crosslink densities. The inset shows the circuit model used for fitting the data. g) The variations of ionic conductivity and the capacitance of EDL per unit area with crosslink density. h) Property chart of PEEs with different crosslink densities. i) The mass change of the PEE varies with time under a continuous pressure of 100 kPa. The inset shows the PEE and the underlying filter paper before and after the test. The scale bars represent 1 cm. j) Creep strain varies with time under 100 kPa stress. k) Peak strain varies with the number of cycles when subject to a cyclic tension with a maximum stress of 100 kPa. l) Peak stress varies with the number of cycles when subjected to a cyclic tension with a maximum strain of 20%. The insets in (j), (k), and (l) show the corresponding loading profiles. The PEEs in (i), (j), (k), and (l) contain 1.5% HDDA.

the crosslink density due to the shorter average polymer chains at larger crosslink densities (Figure 2c). The strength increases and then decreases with the crosslink density, peaking at 424.0 kPa at 1.5% HDDA. The reduction of strength is caused by the limited fracture strain. Decent strength is required for demolding the PEE from the silicon wafer without cracking.

Besides the bulk properties, the adhesion property of PEE is also important. In general, a weak adhesion is demanded for the PEE for easy demolding from the silicon wafer and facilitating the recovery of the ionotronic sensor, whose operation encounters the adhesion force between the PEE and the upper electrode.[30] We perform tack tests to probe the adhesion between various P([BMIM][SPA]-*co*-MA) elastomers and ITO/PET electrode (Figure 2d). Overall, both the adhesion strength and the adhesion energy decrease with the crosslink density (Figure 2e), because P([BMIM][SPA]-*co*-MA) networks mainly adhere to the ITO/PET electrode through molecular interaction that tapers off as the polymer chains get shorter.

We next characterize the electrical properties using an impedance analyzer. Figure 2f shows the Nyquist plots and the inset shows the equivalent circuit model used to fit the data. Both the ionic conductivity $\sigma$ and the unit-area EDL capacitance $c_{EDL}$ decrease with the crosslink density (Figure 2g), due to the worse chain mobility at larger crosslink densities.[39] $\sigma$ varies from 3.23 to 9.91 mS m$^{-1}$ and $c_{EDL}$ varies from 0.64 to 3.82 nF mm$^{-2}$. A higher $\sigma$ gives a lower $RC$ delay and a larger $c_{EDL}$ yields a larger absolute capacitance. We compare the mechanical and electrical properties of P([BMIM][SPA]-*co*-MA) elastomers with different crosslink densities in the property chart (Figure 2h). To make a balance, we will set the crosslink density at 1.5% in the following.

The P([BMIM][SPA]-*co*-MA) elastomer exhibits marked stability. A PEE sample maintains mass stably without leakage (Figure 2i) when subjected to a constant pressure of 100 kPa in the open air with fluctuating temperature and relative humidity (Figure S2, Supporting Information) over 1 week. Besides, the ionic conductivity of the PEE remains mostly constant in the open air over 7 days (Figure S3, Supporting Information). Under the tensile creep test with a constant stress of 100 kPa, the PEE maintains strain, ≈18.2%, stably over 4000 s (Figure 2j). Under the load-controlled cyclic fatigue test with a constant peak stress of 100 kPa, the PEE mostly maintains a constant peak strain of ≈20.4% over 1000 cycles (Figure 2k). Under the displacement-controlled cyclic fatigue test with a constant peak strain of 20%, the PEE mostly maintains a constant peak stress of ≈106 kPa over 1000 cycles (Figure 2l). These results signify the excellent stability and fatigue resistance of the P([BMIM][SPA]-*co*-MA) elastomer, which lays a solid foundation for the excellent durability and robustness of the ionotronic sensor.

We then use the optimized P([BMIM][SPA]-*co*-MA) elastomer to fabricate ionotronics sensors and measure their normalized relative capacitance change, $\Delta C/C_0$, with pressure, where $\Delta C$ is the capacitance change and $C_0$ is the initial capacitance. We use the PEEs with various base lengths ($b$) and spacings ($d$) (Figure S4, Supporting Information) to investigate the effects of the geometries of the micropyramids on the sensing performances. **Figure 3a** displays the variations of $\Delta C/C_0$ with pressure for the sensors with different spacings and a base length of 20 µm, and Figure 3b displays the variations of $\Delta C/C_0$ with pressure for the sensors with different base lengths and a spacing of 200 µm. Remarkably, $\Delta C/C_0$ varies over five orders of magnitude, from $10^{-1}$ to $10^4$. The large magnitude of the capacitance provides a large tolerance to the parasitic capacitance/noise signal. Sensitivity is calculated as the tangent of the $\Delta C/C_0$-$P$ curve, $\delta(\Delta C/C_0)/\delta P$, where $P$ is the applied pressure. The maximum sensitivities of different geometries are collected in Figure 3c, in which the ionotronic sensor with $b_{20}d_{200}$ and a base angle of 54.7° exhibits the highest value of 69.6 kPa$^{-1}$. The high sensitivities potentialize the ionotronic sensor in broad applications, e.g., pulse-wave monitoring (Figure S5, Supporting Information). Furthermore, the ionotronic sensor has an upper sensing limit on the order of 1 MPa and maintains sensing performances well within the high-pressure range. Specifically, a high sensitivity of 4.96 kPa$^{-1}$ is achieved at a pressure of 500 kPa. The sensor maintains sensing performances well over 4 months (Figure S6, Supporting Information), and it still senses finger touch well when exposed to human sweat (Figure S7, Supporting Information).

We carry out finite element analysis (FEA) to lucubrate the working mechanism of the ionotronic sensor with $b_{20}d_{200}$. At the undeformed state, the upper electrode is separated from the PEE by air (Figure 3d). When a low pressure, e.g., 10 kPa, is applied, the upper electrode deflects and contacts the tips of the micropyramids in the middle (Figure 3e), forming distributed EDLs and significantly boosting the capacitance. The deformation is inhomogeneous that the central micropyramids deform more than the peripheral ones. When a high pressure, e.g., 1 MPa, is applied, all micropyramids are severely deformed (Figure 3f). The capacitance plateaus since the upper electrode is almost in full contact with the flattened PEE and the contact area barely increases with pressure (Figure S8, Supporting Information), which is consistent with the tendencies in Figure 3a,b.

Recall the optimized elasticity of the PEE, which is further enhanced by the voids of the micropyramids,[18] and the low adhesion between the upper electrode and the PEE. These attributes are beneficial for the response speed and the durability of the ionotronic sensor. We test the response speed by knocking the ionotronic sensor with a hammer, corresponding to an instantaneous pressure of ≈400 kPa. Both the response time and the recovery time of the sensor reach ≈6 ms (Figure 3g). Under the cyclic loading with a peak pressure of 300 kPa and a frequency of 0.5 Hz, the sensor exhibits stable output signals with negligible signal drift over 30 000 cycles (Figure 3h). Under the static pressure of 500 kPa, the sensor holds a stable capacitance of ≈16.28 nF over 4000 s (Figure 3i). We compare the sensitivity (Figure 3j) and the maximum $\Delta C/C_0$ (Figure 3k) of our ionotronic sensor with those of other capacitive pressure sensors using microstructured dielectric layers, either solvent-free (e.g., PDMS) or solvent-leakage (e.g., ionogel). It is clear that the microstructured PEE-based ionotronic sensor unifies the merits of high sensitivity and large magnitude of capacitance meanwhile overcoming the drawback of leakage for excellent long-term stability.

Ionotronic sensors with excellent stability and high sensitivities, especially over a broad high-pressure range, are promising for tactile sensing. We first demonstrate their application for a wearable keyboard. The system consists of, e.g., two sensors, a 28-bit multichannel capacitance-to-digital converter (CDC), a microcontroller unit (MCU), and a computer with a screen (**Figure 4a**). The sensors are worn on the arm of the user and connected

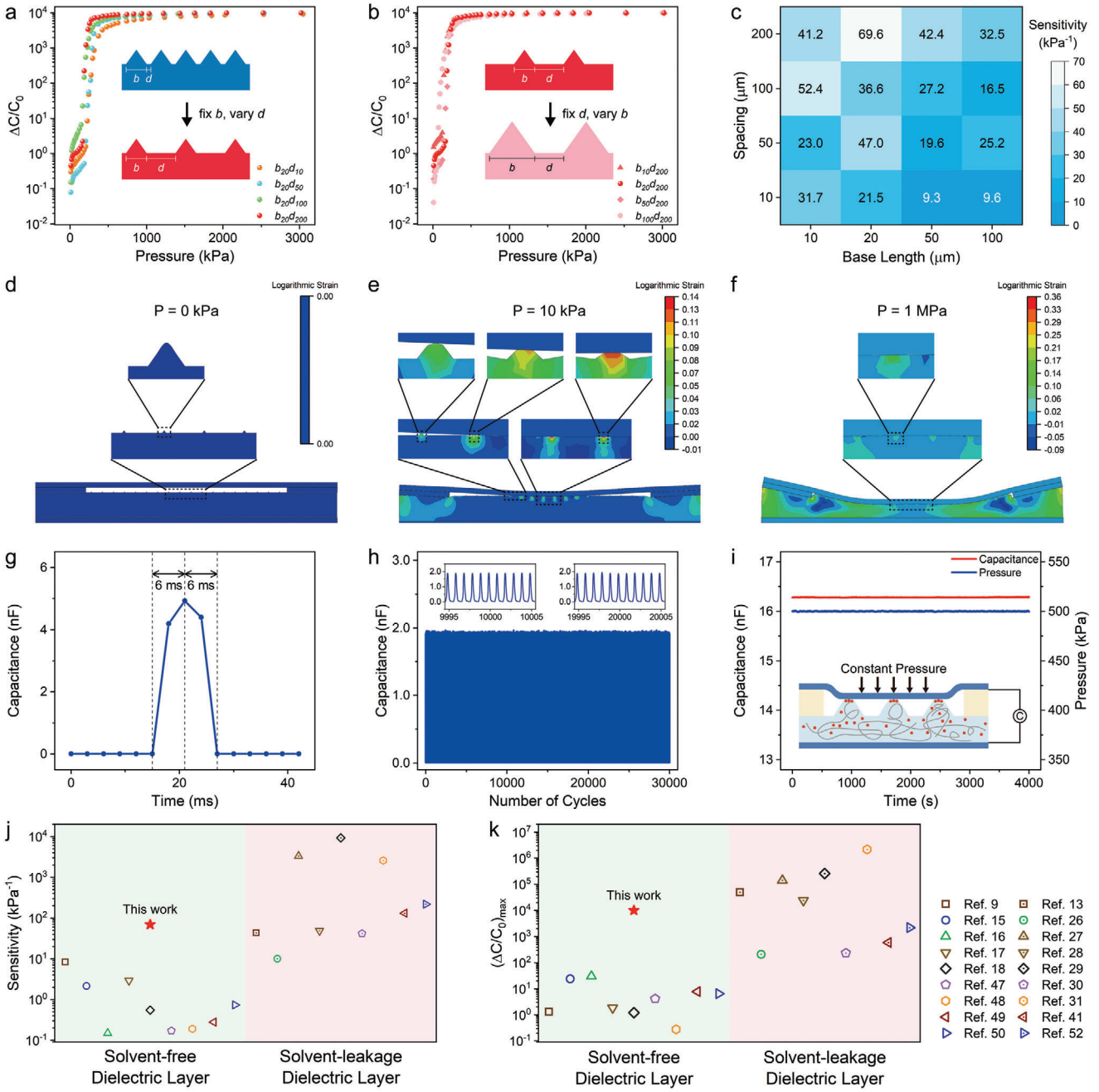


**Figure 3.** Performances of the ionotronic sensor. a) The variations of $\Delta C/C_0$ with pressure when the base length is fixed at 20 μm. $b_x d_y$ means that the micropyramid has a base length of $x$ μm and a spacing of $y$ μm. b) The variations of $\Delta C/C_0$ with pressure when the spacing is fixed at 200 μm. c) Sensitivity map with different base lengths and spacings. Finite element simulations of the sensor with a base length of 20 μm and a spacing of 200 μm under d) zero pressure, e) 10 kPa, and f) 1 MPa. The deformation states of the micropyramids under different pressures are magnified. g) The response of the sensor when subject to a transient load of ≈400 kPa. h) Capacitance as a function of the number of cycles under a dynamic compression with a maximum pressure of ≈300 kPa. i) Capacitance varies with time when subject to a constant pressure of ≈500 kPa. Comparison of j) sensitivity and k) maximum $\Delta C/C_0$ of this work with other works with either solvent-free[9,15–18,47–50] or solvent-leakage[13,26–31,51,52] dielectric layers.

to the CDC, which converts the capacitance values to digital values and stores them in the registers. The MCU reads the digital values through the inter-integrated circuit and processes them, and sends the coded characters to the computer. Remarkably, the large range of the capacitance of the sensor enables a brand-new coding strategy in that every sensor can be coded with multiple commands without signal interferences. For example, each sensor can generate four commands based on long/short and slight/heavy press (Figure 4b). Figure 4c shows the capacitance pattern and the corresponding digital signals of one sensor. The signals can be applied to control the expressions of a live2D character (Figure 4d; and Movie S1, Note S1,

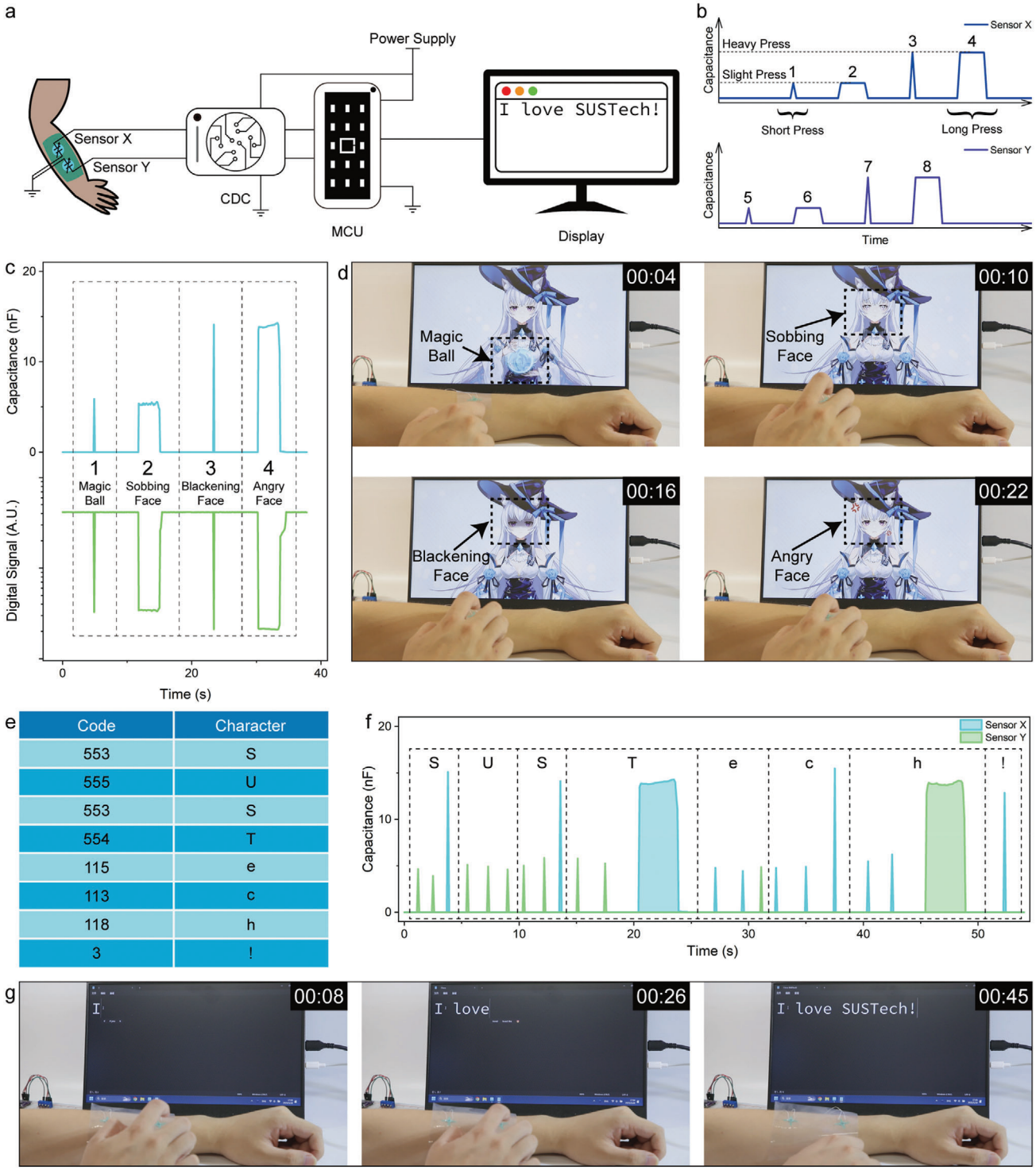


**Figure 4.** Ionotronic sensors for a wearable keyboard. a) Schematic of the system consisting of ionotronic sensors connected to a CDC, which is in turn connected to an MCU to display information on a screen. b) Schematic of the coding of different pressing actions. c) Real-time signal pattern of one sensor and the corresponding commands to control a cartoon character. d) Responses of the cartoon character to the signals. The authors own the copyright of the cartoon character. e) Selected coding based on the combination of the signals from two sensors. f) Real-time signal pattern of two sensors and the corresponding commands for typing. g) Demonstration of typing based on the wearable keyboard.

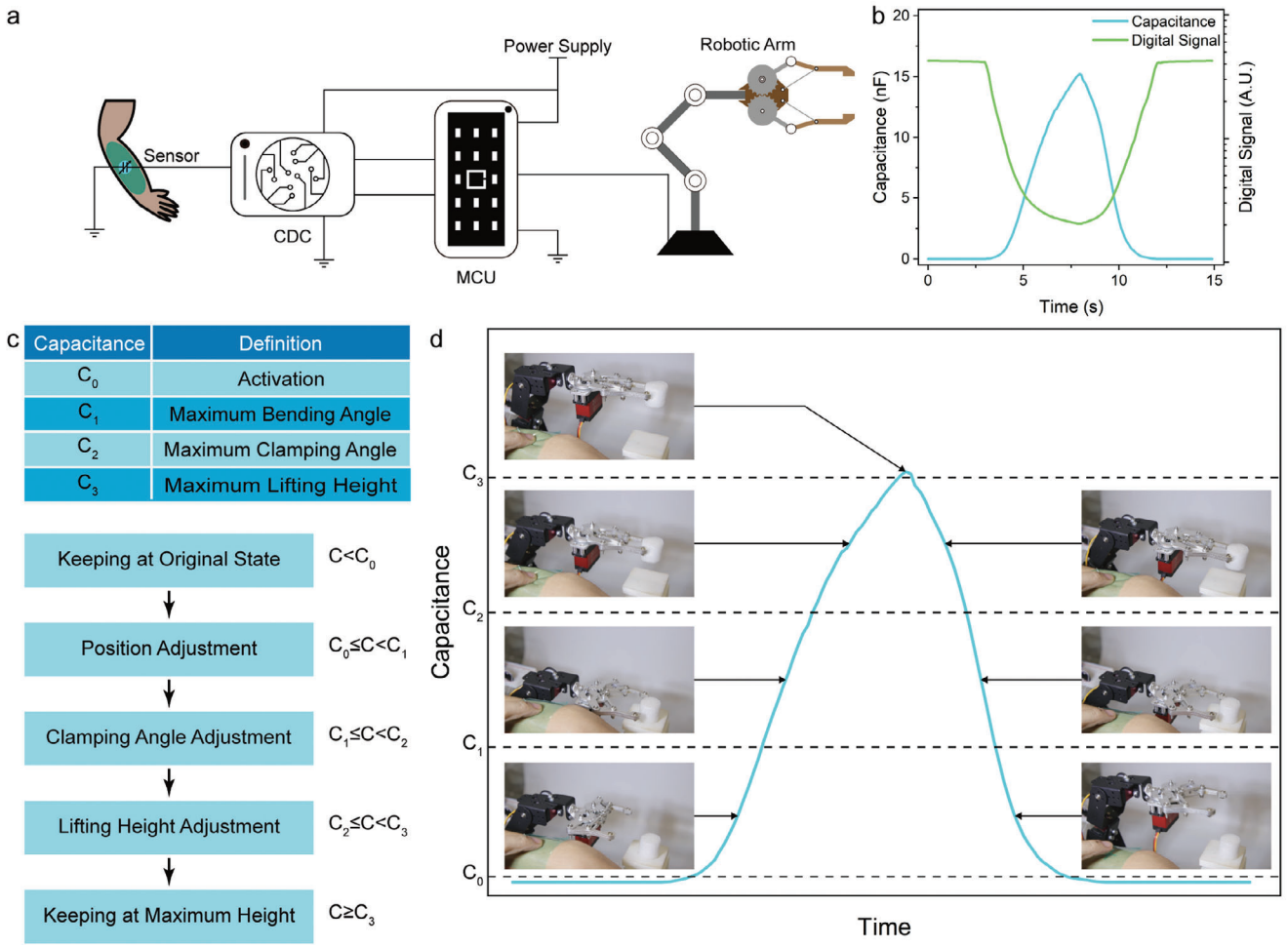


**Figure 5.** Ionotronic sensors for controlling a robotic manipulator. a) Schematic of the system, in which the controlling command from the MCU is sent to a robotic manipulator. b) Representative real-time capacitance pattern of the sensor and the corresponding digital signal generated by the CDC. c) Definition of the controlling logic. d) Demonstration of controlling the movements of the robotic manipulator by regulating the capacitance of the ionotronic sensor.

Supporting Information). Figure 4e tabulates selected codes and the corresponding characters based on the combination of the signals from two sensors. The real-time signal of the typing is plotted in Figure 4f. After processing, the screen of the computer displays the sentence "I love SUSTech!" (Figure 4g; and Movie S2, Note S2, Supporting Information).

We further demonstrate the application of the ionotronic sensor as a wearable quasicontinuous controller for a robotic arm. We use one ionotronic sensor and connect the output ports of the MCU to the digital servos of a robotic arm (**Figure 5a**). We gradually increase the pressure until the capacitance increases from ≈3 pF to 15 nF, and then release the pressure. The obtained mapping relation is plotted in Figure 5b. The ultrabroad capacitance range allows the division of the signal into multiple intervals, each corresponding to a command. We set four critical capacitances ($C_0$, $C_1$, $C_2$, $C_3$), corresponding to the operations of activation, maximum bending angle, maximum clamping angle, and maximum lifting height (Figure 5c). When the capacitance is lower than $C_0$, $C<C_0$, the robotic arm keeps at its original state. When $C_0 \leq C<C_1$, the robotic arm adjusts its position and approaches a cylindrical foam. When $C_1 \leq C<C_2$, the robotic arm adjusts its clamping angle to the maximum to grip the cylindrical foam tightly. When $C_2 \leq C<C_3$, the robotic arm lifts the cylindrical foam from the stage to the maximum lifting height. When $C_3 \leq C$, the robotic arm keeps at the maximum height. When the capacitance decreases, the robotic arm reverses the operations. Benefiting from the ultrabroad capacitance range and the high sensitivities over a broad high-pressure range, the five intervals are sufficiently wide such that the corresponding commands do not interfere with each other. Figure 5d shows the capacitance-time curve with the corresponding snapshots of various operations, which run smoothly (Movie S3 and Note S3, Supporting Information).

In general, microstructures of different kinds, [40–42] such as porous microstructures, microcylinders, microspheres, and graded intrafillable architectures, could be used to enhance the sensing performance of tactile sensors, e.g., sensitivity. Pyramidal microstructures have been used in this work owing to the relatively mild fabrication condition, ≈70 °C potassium hydroxide solution, and the effectiveness in increasing the sensitivity and

decreasing the response time. Compared to the molding process, mold-free fabrication techniques are more economical and offer a higher degree of design flexibility.[43–45] For example, multimaterial 3D printing enables on-demand construction of 3D structures for either the ionic conductors[46] or the whole ionotronic sensors.[34] For the wearable keyboard, only eight combinations of the signals from two sensors have been coded. However, more characters are feasible with more sensors to reproduce all keys of a real keyboard such that the wearable keyboard can be used, e.g., for deaf-mute patients, for daily communications. Besides, only long/short and slight/heavy presses have been coded for typing, more commands can be coded in future studies by further dividing the ultrabroad ranged signal spatially and temporally for more sophisticated coding and controlling.

## 3. Conclusion

To sum up, we have reported an ionotronic sensor with high sensitivities and excellent stability by using a microstructured leakage-free PEE. With optimized mechanical and electrical properties of the PEE and the geometrical parameters of the micropyramids, the ionotronic sensor achieves a high sensitivity of 69.6 $kPa^{-1}$ and maintains functions stably under static and dynamic fatigue loads. The broad sensing range within the high-pressure realm enables a brand-new coding strategy. The applications of the sensor as a wearable keyboard for typing and a quasi-continuous controller for a robotic arm have been demonstrated. Leakage-free microstructured ionic conductors-based ionotronic sensors have enormous potential for high-performance artificial skins.

## 4. Experimental Section

*Materials*: 1-butyl-3-methylimidazolium chloride ([BMIM]Cl, 97%), 3-sulfopropyl methacrylate potassium salt (K[SPA], 98%), 4-methoxyphenol (MEHQ, 99%), 1,6-hexanediol diacrylate (HDDA 90%) were purchased from Sigma-Aldrich. Methyl acrylate (MA, 99%) was purchased from Macklin. Acetonitrile (ACN, 99.9%, super dry, with molecular sieves) was purchased from J&K Scientific. Photoinitiator 1173 (I-1173) was purchased from Shanghai Yinchang New Material Co., Ltd. Indium tin oxide coated polyethylene terephthalate (ITO/PET) was purchased from Shenzhen SIMIHUI Electronic Material Co., Ltd. Polydimethylsiloxane (PDMS) film was purchased from Zhongke Materials Co., Ltd. Polyimide (PI) tape was purchased from 3 M.

*Synthesis of [BMIM][SPA]*: [BMIM]Cl (13.97 g), K[SPA] (18.58 g), MEHQ (18.6 mg), and ACN (56 mL) were mixed in a beaker and stirred at room temperature for 24 h. After that, the precipitate was filtered out and ACN was removed using a rotary evaporator. The obtained liquid was further dried at ≈5 Pa at room temperature overnight to remove ACN and water completely. Finally, [BMIM][SPA] was obtained and stored at a low temperature (≈5 °C) in a refrigerator.

*Preparation of PEE*: First, [BMIM][SPA] (3.32 g), MA (2.58 g), HDDA (45.3, 90.5, 136, 181, or 226 mg for different cross-linking densities), and I-1173 (0.1 mL, 0.2 M in ACN solution,) were mixed to form the PEE precursor. The precursor was injected into a mold, made of two pieces of released film separated by a silicone spacer, and cured under UV light with a wavelength of 365 nm for 2 h at room temperature. The obtained P([BMIM][SPA]-*co*-MA) was annealed in an oven at 60 °C for 2 h to remove residual solvent.

*Mechanical Properties of PEE*: Mechanical properties of PEE were characterized using a universal testing machine (Instron 68SC-1, 500 N load cell) at room temperature and a humidity of ≈50%. For the uniaxial tensile test, PEE was cut into dumbbell shapes with a gauge length of 15 mm, a gauge width of 3 mm, and a thickness of 1 mm. The loading velocity was fixed at 15 mm $min^{-1}$. Force-displacement curves were recorded and the fracture strain and strength were determined from the failure points. Elastic modulus was determined as the averaged slope over ≈1–5% strain of the nominal stress-nominal strain curves. For the tack test, PEE was cut into disk shapes with a diameter of 20 mm and a thickness of 0.5 mm. The probe was a flat disk of ITO/PET electrode with a diameter of 15 mm. The probe was loaded at 0.3 mm $min^{-1}$ to 60 N, held for 1 min, and then unloaded at 1 mm $s^{-1}$ until the probe was detached from the sample. Force-displacement curves were recorded and the adhesive strength was calculated as the peak force divided by the area of the probe and the adhesive energy was defined as the integral of force versus displacement up to the peak force divided by the area of the probe. For the stability test, PEE was cut into disk shapes with a diameter of 12 mm and a thickness of 1 mm, placed on a piece of filter paper as the substrate, and subjected to a constant pressure of 100 kPa for 1 week. The mass of the PEE was measured every day. For the creep test, PEE was cut into the same shapes as that in the uniaxial tensile test, and subjected to a constant loading with a stress of 100 kPa for 4000 s. For the fatigue test, PEE was cut into the same shapes as that in the uniaxial tensile test, and subjected to a cyclic loading with a peak stress of 100 kPa or a peak strain of 20% for 1000 cycles at a frequency of 1 Hz. Engineering stress and engineering strain are used unless otherwise specified.

*Electrical Properties of PEE*: Electrical properties of PEE were characterized using an impedance analyzer (Keysight E4990A) in the frequency range of 1 kHz to 20 MHz and at a voltage of 0.5 V. A 1 mm thick PEE was dried at 60 °C overnight and then two layers of 50 nm thick gold films were sputtered on the two sides of the PEE by ion beam sputtering. The sputtered PEE was cut into rectangular shapes with a length of 10 mm and a width of 4 mm. Finally, the two electrodes were connected to the impedance analyzer for the measurement. ZView 3.1 software was used to analyze the data to calculate the ionic conductivity of the PEE and the EDL capacitance.

*Preparation of Silicon Mold*: The photolithography technique was used to fabricate the silicon mold. A double-oxidized (001) 4 in. silicon wafer (with an oxide thickness of 500 nm) was first washed for 10 min using a mixed solution of the ammonia and hydrogen peroxide (with a volume ratio of ≈1:1) under ≈70 °C and then washed for 10 min using a mixed solution of the hydrochloric acid and hydrogen peroxide (with a volume ratio of ≈1:1) under ≈70 °C to remove the impurities. After each process, the wafer was ultrasonically cleaned for 15 min in fresh DI water to remove the residual. A 1.2 µm thick RZJ-304-10 photoresist mask with a designated pattern was coated on the wafer using a mask aligner (SUSS MA6). After a hard baking process (120 °C, 30 min), the wafer was soaked in an etching solution containing hydrofluoric acid (BOE ≈6:1) to etch the exposed silicon dioxide (with an etching speed of ≈100 nm $min^{-1}$ and an etching time of 310 s), forming silicon dioxide grids on the wafer. Then, the photoresist mask was cleaned by using the SYS9070 photoresist removal solution. Finally, the silicon wafer was treated with a potassium hydroxide solution (with a concentration of ≈25 wt% and a temperature of ≈70 °C) to form square pyramid cavity arrays.

*Fabrication of Ionotronic Sensor*: The PEE precursor was injected into a mold made of the microstructured silicon wafer and a PET release film with a 0.2 mm thick silicone spacer. After curing (365 nm UV light for 2 h) and drying (60 °C in the oven overnight), the PEE was carefully peeled off from the silicon wafer and cut into a disk with a diameter of 6 mm, with the micropyramid array located at the center with a diameter of 4 mm. A 0.2 mm thick PET ring with an outer diameter of 6 mm and an inner diameter of 4 mm was cut as the spacer. An ITO/PET film with a thickness of 0.125 mm, a diameter of 6 mm, and a sheet resistance of 5 Ω $sq^{-1}$ was cut into disk shape as the electrode. The electrodes, the PEE, and the spacer were stacked as shown in Figure 1e and sealed using PET tapes. The electrodes were connected to two copper wires.

*Characterizations of Ionotronic Sensor*: Microstructures on the PEE were observed using the optical microscope (VHX-7000, Keyence). The capacitance of the sensor was measured using a benchtop LCR meter

(TH2838A, Tonghui). The sensor was loaded to the universal testing machine (Instron 68SC-1, 100 N load cell) to measure the sensitivity and to a fatigue testing machine (Instron E3000, 250 N load cell) to measure the stability.

*Finite Element Analysis*: A 2D finite element model of the pressure sensor was built using the commercial finite element software "Abaqus Explicit." Linear quadrilateral elements, i.e., four-node plane stress element (CPS4) were applied to different parts of the sensor. The total numbers of elements and nodes were 4675 and 5299, respectively. Hard normal contact was defined for all contacts between segments to avoid any penetration. The nodes of surfaces in contact were tied together to inhibit any relative movement. The load was applied to the top surface of the upper electrode at a length of 3 mm. All degrees of freedom (DOFs) on the bottom surface of the lower electrode were constrained.

*Signal Acquisition System*: The MCU (ATSAM3×8E, on Arduino DUE microcontroller board) was set to work under the clock frequency of 84 MHz. A four-channel 28-bit CDC (FDC2214, Texas Instruments) was used to read the capacitance of the ionotronic sensor, with a clock frequency of 40 MHz. The capacitance was connected to the input channel of CDC, with an inductance of 18 μH and a capacitance of 33 pF in parallel. The scanning frequency of the system is 10 Hz. The capacitance was acquired by the CDC and stored in the register of the CDC, and then read by the MCU through the inter-integrated circuit ($I^2C$). The signals were further proceeded for the applications of the ionotronic sensor, including a wearable keyboard and a robotic manipulator. For the wearable keyboard, the critical time to identify "long press"/"short press" is 1 s, and the critical capacitance to identify "heavy pressure"/"light pressure" is set as 10 nF. For the wearable quasicontinuous controller for a robotic arm, the critical capacitances ($C_0$, $C_1$, $C_2$, $C_3$) were set as 1, 5, 9, and 14 nF, respectively. The algorithm used the real-time capacitance value of the sensor to identify different pressures and control the robotic arm.

## Supporting Information

Supporting Information is available from the Wiley Online Library or from the author.

## Acknowledgements

The work at Southern University of Science and Technology is supported by National Key Research and Development Program of China (Grant No. 2023YFB3812500), the Natural Science Foundation of China (No. 12302212), the Science, Technology, and Innovation Commission of Shenzhen Municipality (Nos. ZDSYS20210623092005017 and JCYJ20220530114810024), and the Stable Support Plan Program of Shenzhen Natural Science Fund Grant (No. 20200925174603001). The authors acknowledged the assistance of SUSTech Core Research Facilities and the micro and nanofabrication facility of Southern University of Science and Technology for the kind assistance with the lithography process. The authors also thanked Prof. Chuan Fei Guo for the kind assistance with ion plating and Prof. Cong Zhao from Chongqing University of Posts and Telecommunications for valuable discussion and suggestions.

## Conflict of Interest

The authors declare no conflict of interest.

## Data Availability Statement

The data that support the findings of this study are available from the corresponding author upon reasonable request.

## Keywords

artificial skin, ionotronic sensor, microstructure, polyelectrolyte elastomer

Received: October 8, 2023
Revised: December 12, 2023
Published online: December 17, 2023

[1] Y. K. Pang, X. C. Xu, S. E. Chen, Y. H. Fang, X. D. Shi, Y. M. Deng, Z. L. Wang, C. Y. Cao, *Nano Energy* **2022**, *96*, 107572.
[2] G. Li, S. Liu, L. Wang, R. Zhu, *Sci. Robot* **2020**, *5*, eabc8134.
[3] L. Li, Y. Cheng, H. Cao, Z. Liang, Z. Liu, S. Yan, L. Li, S. Jia, J. Wang, Y. Gao, *Nano Energy* **2022**, *95*, 106986.
[4] Y. Cheng, L. Li, Z. Liu, S. Yan, F. Cheng, Y. Yue, S. Jia, J. Wang, Y. Gao, L. Li, *Research* **2022**, *2022*, 9843268.
[5] A. Chortos, J. Liu, Z. Bao, *Nat. Mater.* **2016**, *15*, 937.
[6] B. C.-K. Tee, A. Chortos, A. Berndt, A. K. Nguyen, A. Tom, A. Mcguire, Z. C. Lin, K. Tien, W.-G. Bae, H. Wang, P. Mei, H.-H. Chou, B. Cui, K. Deisseroth, T. N. Ng, Z. Bao, *Science* **2015**, *350*, 313.
[7] Y. Cheng, Y. Xie, H. Cao, L. Li, Z. Liu, S. Yan, Y. Ma, W. Liu, Y. Yue, J. Wang, Y. Gao, L. Li, *Chem. Eng. J.* **2023**, *453*, 139823.
[8] Q. Lin, J. Huang, J. Yang, Y. Huang, Y. Zhang, Y. Wang, J. Zhang, Y. Wang, L. Yuan, M. Cai, X. Hou, W. Zhang, Y. Zhou, S. G. Chen, C. F. Guo, *Adv. Healthcare Mater.* **2020**, *9*, e2001023.
[9] G. Schwartz, B. C.-K. Tee, J. Mei, A. L. Appleton, D. H. Kim, H. Wang, Z. Bao, *Nat. Commun.* **2013**, *4*, 1859.
[10] Y. Cheng, Y. Xie, Z. Liu, S. Yan, Y. Ma, Y. Yue, J. Wang, Y. Gao, L. Li, *ACS Nano* **2023**, *17*, 1393.
[11] X. Yu, Z. Xie, Y. Yu, J. Lee, A. Vazquez-Guardado, H. Luan, J. Ruban, X. Ning, A. Akhtar, D. Li, B. Ji, Y. Liu, R. Sun, J. Cao, Q. Huo, Y. Zhong, C. Lee, S. Kim, P. Gutruf, C. Zhang, Y. Xue, Q. Guo, A. Chempakasseril, P. Tian, W. Lu, J. Jeong, Y. Yu, J. Cornman, C. Tan, B. Kim, et al., *Nature* **2019**, *575*, 473.
[12] S. Pyo, J. Lee, K. Bae, S. Sim, J. Kim, *Adv. Mater.* **2021**, *33*, 2005902.
[13] R. Yang, A. Dutta, B. Li, N. Tiwari, W. Zhang, Z. Niu, Y. Gao, D. Erdely, X. Xin, T. Li, H. Cheng, *Nat. Commun.* **2023**, *14*, 2907.
[14] R. Li, Y. Si, Z. Zhu, Y. Guo, Y. Zhang, N. Pan, G. Sun, T. Pan, *Adv. Mater.* **2017**, *29*, 1700253.
[15] Z. Feng, Q. He, X. Wang, Y. Lin, J. Qiu, Y. Wu, J. Yang, *ACS Appl. Mater. Interfaces* **2023**, *15*, 6217.
[16] Y. Zhang, J. Yang, X. Hou, G. Li, L. Wang, N. Bai, M. Cai, L. Zhao, Y. Wang, J. Zhang, K. Chen, X. Wu, C. Yang, Y. Dai, Z. Zhang, C. F. Guo, *Nat. Commun.* **2022**, *13*, 1317.
[17] Z. Guo, L. Mo, Y. Ding, Q. Zhang, X. Meng, Z. Wu, Y. Chen, M. Cao, W. Wang, L. Li, *Micromachines* **2019**, *10*, 206.
[18] S. C. B. Mannsfeld, B. C.-K. Tee, R. M. Stoltenberg, C. V. H.-H. Chen, S. Barman, B. V. O. Muir, A. N. Sokolov, C. Reese, Z. Bao, *Nat. Mater.* **2010**, *9*, 859.
[19] J.-H. Zhang, Z. Li, J. Xu, J. Li, K. Yan, W. Cheng, M. Xin, T. Zhu, J. Du, S. Chen, X. An, Z. Zhou, L. Cheng, S. Ying, J. Zhang, X. Gao, Q. Zhang, X. Jia, Y. Shi, L. Pan, *Nat. Commun.* **2022**, *13*, 5839.
[20] S. R. A. Ruth, L. Beker, H. Tran, V. R. Feig, N. Matsuhisa, Z. Bao, *Adv. Funct. Mater.* **2019**, *30*, 1903100.
[21] C. H. Yang, *Appl. Phys. Lett.* **2023**, *122*, 070501.
[22] C. Yang, Z. Suo, *Nat. Rev. Mater.* **2018**, *3*, 125.
[23] Y. Chang, L. Wang, R. Li, Z. Zhang, Q. Wang, J. Yang, C. F. Guo, T. Pan, *Adv. Mater.* **2021**, *33*, 2003464.
[24] B. Nie, R. Li, J. D. Brandt, T. Pan, *Lab Chip* **2014**, *14*, 1107.
[25] B. Nie, R. Li, J. Cao, J. D. Brandt, T. Pan, *Adv. Mater.* **2015**, *27*, 6055.
[26] K. L. Kim, S. H. Cho, J.-B. Lee, G. Kim, K. Lee, S. W. Lee, H. S. Kang, C. Park, J.-H. Ahn, W. Shim, I. Bae, C. Park, *ACS Appl. Mater. Interfaces* **2023**, *15*, 19319.
[27] N. Bai, L. Wang, Q. Wang, J. Deng, Y. Wang, P. Lu, J. Huang, G. Li, Y. Zhang, J. Yang, K. Xie, X. Zhao, C. F. Guo, *Nat. Commun.* **2020**, *11*, 209.

 

[28] N. Bai, L. Wang, Y. Xue, Y. Wang, X. Hou, G. Li, Y. Zhang, M. Cai, L. Zhao, F. Guan, X. Wei, C. F. Guo, *ACS Nano* **2022**, *16*, 4338.
[29] Q. Liu, Y. Liu, J. Shi, Z. Liu, Q. Wang, C. F. Guo, *Nanomicro Lett.* **2021**, *14*, 21.
[30] S. H. Cho, S. W. Lee, S. Yu, H. Kim, S. Chang, D. Kang, I. Hwang, H. S. Kang, B. Jeong, E. H. Kim, S. M. Cho, K. L. Kim, H. Lee, W. Shim, C. Park, *ACS Appl. Mater. Interfaces* **2017**, *9*, 10128.
[31] Z. Chen, Y. Zhang, B. Zhu, Y. Wu, X. Du, L. Lin, D. Wu, *ACS Appl. Mater. Interfaces* **2022**, *14*, 19672.
[32] T. A. Shmool, L. K. Martin, A. Jirkas, R. P. Matthews, A. P. Constantinou, D. M. Vadukul, T. K. Georgiou, F. A. Aprile, J. P. Hallett, *Chem. Mater.* **2023**, *35*, 5798.
[33] X. Fan, S. Liu, Z. Jia, J. J. Koh, J. C. C. Yeo, C.-G. Wang, N. E. Surat'man, X. J. Loh, J. Le Bideau, C. He, Z. Li, T.-P. Loh, *Chem. Soc. Rev.* **2023**, *52*, 2497.
[34] C. Li, J. Cheng, Y. He, X. He, Z. Xu, Q. Ge, C. Yang, *Nat. Commun.* **2023**, *14*, 4853.
[35] H. J. Kim, B. Chen, Z. Suo, R. C. Hayward, *Science* **2020**, *367*, 773.
[36] S. W. Lee, J. Jang, Y. Kim, S. Lee, K. Lee, H. Han, H. Lee, J. W. Oh, H. Kim, T. Kim, M. D. Dickey, C. Park, *Appl. Phys. Rev.* **2022**, *9*, 041404.
[37] B. Yang, W. Yuan, *ACS Appl. Mater. Interfaces* **2019**, *11*, 40620.
[38] S. Xu, J.-X. Yu, H. Guo, S. Tian, Y. Long, J. Yang, L. Zhang, *Nat. Commun.* **2023**, *14*, 219.
[39] C. A. Angell, *Solid State Ionics* **1983**, *3*, 9.
[40] X. Cui, F. Huang, X. Zhang, P. Song, H. Zheng, V. Chevali, H. Wang, Z. Xu, *iScience* **2022**, *25*, 104148.
[41] J. Shi, Y. Dai, Y. Cheng, S. Xie, G. Li, Y. Liu, J. Wang, R. Zhang, N. Bai, M. Cai, Y. Zhang, Y. Zhan, Z. Zhang, C. Yu, C. F. Guo, *Sci. Adv.* **2023**, *9*, eadf8831.
[42] Y. Luo, J. Shao, S. Chen, X. Chen, H. Tian, X. Li, L. Wang, D. Wang, B. Lu, *ACS Appl. Mater. Interfaces* **2019**, *11*, 17796.
[43] Q. Ge, Z. Q. Li, Z. L. Wang, K. Kowsari, W. Zhang, X. N. He, J. L. Zhou, N. X. Fang, *Int. J. Extrem. Manuf.* **2020**, *2*, 022004.
[44] P. Zhang, Q. Li, Y. Xiao, C. Yang, *ACS Appl. Electron. Mater.* **2020**, *3*, 668.
[45] J. Li, J. Cao, B. Lu, G. Gu, *Nat. Rev. Mater.* **2023**, *8*, 604.
[46] C. Zhang, H. Zheng, J. Sun, Y. Zhou, W. Xu, Y. Dai, J. Mo, Z. Wang, *Adv. Mater.* **2022**, *34*, 2105996.
[47] J. Wang, R. Suzuki, M. Shao, F. Gillot, S. Shiratori, *ACS Appl. Mater. Interfaces* **2019**, *11*, 11928.
[48] Z. Li, S. Zhang, Y. Chen, H. Ling, L. Zhao, G. Luo, X. Wang, M. C. Hartel, H. Liu, Y. Xue, R. Haghniaz, K. Lee, W. Sun, H. Kim, J. Lee, Y. Zhao, Y. Zhao, S. Emaminejad, S. Ahadian, N. Ashammakhi, M. R. Dokmeci, Z. Jiang, A. Khademhosseini, *Adv. Funct. Mater.* **2020**, *30*, 2070326.
[49] Q. Zhou, B. Ji, Y. Wei, B. Hu, Y. Gao, Q. Xu, J. Zhou, B. Zhou, *J. Mater. Chem. A* **2019**, *7*, 27334.
[50] A. Chhetry, S. Sharma, H. Yoon, S. Ko, J. Y. Park, *Adv. Funct. Mater.* **2020**, *30*, 1910020.
[51] A. Chhetry, J. Kim, H. Yoon, J. Y. Park, *ACS Appl. Mater. Interfaces* **2019**, *11*, 3438.
[52] X. Lin, H. Xue, F. Li, H. Mei, H. Zhao, T. Zhang, *ACS Appl. Mater. Interfaces* **2022**, *14*, 31385.